

Distribution Prototype Diffusion Learning for Open-set Supervised Anomaly Detection

Fuyun Wang, Tong Zhang, Yuanzhi Wang, Yide Qiu, Xu Guo
School of Computer Science and Engineering
Nanjing University of Science and Technology

fyw271828@njust.edu.cn, tong.zhang@njust.edu.cn, yuanzhiwang@njust.edu.cn,
121106010824@njust.edu.cn, guo.xu@njust.edu.cn

Xin Liu
SeetaCloud Technology
Nanjing, China
xin.liu@seetacloud.com

Zhen Cui
School of Artificial Intelligence
Beijing Normal University
zhen.cui@bnu.edu.cn

Abstract

In Open-set Supervised Anomaly Detection (OSAD), the existing methods typically generate pseudo anomalies to compensate for the scarcity of observed anomaly samples, while overlooking critical priors of normal samples, leading to less effective discriminative boundaries. To address this issue, we propose a Distribution Prototype Diffusion Learning (DPDL) method aimed at enclosing normal samples within a compact and discriminative distribution space. Specifically, we construct multiple learnable Gaussian prototypes to create a latent representation space for abundant and diverse normal samples and learn a Schrödinger bridge to facilitate a diffusive transition toward these prototypes for normal samples while steering anomaly samples away. Moreover, to enhance inter-sample separation, we design a dispersion feature learning way in hyperspherical space, which benefits the identification of out-of-distribution anomalies. Experimental results demonstrate the effectiveness and superiority of our proposed DPDL, achieving state-of-the-art performance on 9 public datasets.

1. Introduction

Anomaly detection (AD) [15, 21, 42, 44] aims to identify outliers significantly diverging from the prevailing samples in a dataset, and has a wide range of applications like industrial inspection, medical image analysis, and scientific discovery, etc. Recently, unsupervised anomaly detection (UAD) [6, 11, 26, 28] and few-shot anomaly detection (FSAD) [12, 21, 22] have emerged as prominent research paradigms, emphasizing the modeling of normal sample distributions to discern anomalies effectively. Yet,

these methods often neglect prior knowledge from limited anomaly samples, resulting in imprecise delineation of normal sample boundaries and reduced efficacy in differentiating normal from anomaly instances. On the contrary, supervised anomaly detection (SAD) [2, 20, 41] leverages a limited subset of anomaly samples as prior knowledge, improving detection performance. However, this reliance on seen anomalies poses a risk of overfitting and hampers generalization to unseen anomalies in real-world settings.

To mitigate the challenge of limited generalization inherent in closed-set training, we focus on open-set supervised anomaly detection (OSAD) [1, 27, 45, 46], which utilizes a small set of known anomaly classes during training to identify unseen anomalies from open-set classes. By leveraging prior knowledge from observed samples, OSAD methods could reduce false positive errors. To improve the generalized detection of unseen anomalies, DRA [9] leverages data augmentation and outlier exposure to learn a decomposed anomaly representation comprising seen anomalies, pseudo-anomalies, and potential residual anomalies. BGAD [41] leverages decision boundaries derived from normalized flow models to capture and model anomaly information. Recently, AHL [45] simulates heterogeneous anomaly distributions and performs collaborative differentiable learning to further enhance the model’s generality.

While data augmentation and outlier exposure techniques [9, 19, 33] have demonstrated considerable success in anomaly detection, they fall short in generating comprehensive pseudo anomalies, capturing only a fraction of potential unseen anomalies. This limitation arises from overlooking the intricate nature of real-world anomaly distributions, thereby hindering the model’s ability to generalize to novel anomaly types. Although AHL [45] has

made strides in addressing this issue by simulating heterogeneous anomaly distributions, it still relies on approximating unknown out-of-distribution anomalies using known in-distribution anomalies for generalization. Yet, three critical issues persist: i) the simulation mechanism cannot cover all anomaly distribution patterns due to the varied scales and structures of anomaly distributions; ii) simulated anomalies inherit in-distribution data biases, leading to suboptimal performance on out-of-distribution anomalies; iii) the diversity of normal samples presents dilemmas for existing methods, complicating the differentiation between normal and anomaly boundaries. These issues prompt a fundamental question: *Instead of generating pseudo and uncertain anomaly samples, how can we accurately characterize compact distribution boundaries amidst a range of diverse normal samples and achieve robust generalization for unknown out-of-distribution anomalies?*

To address the aforementioned issue, in this work, we propose a Distribution Prototype Diffusion Learning (DPDL) method for open-set supervised anomaly detection. Considering abundant and diverse normal samples but very limited anomaly data, our method involves learning latent distribution prototypes, specifically multiple Gaussian distributions, onto which all observed normal samples can be effectively projected. To facilitate the mapping of normal samples into the prototype space, we leverage Schrödinger bridge (SB) framework, which enables a diffusive transition by aligning the distributions of these samples with the prototypes. The SB-based diffusion way could mitigate the out-of-distribution issue for normal samples to some extent. Within the distribution prototype space, we push observed anomaly samples away from normal samples to enhance discriminative capacity. Notably, both the prototypes and the diffusive bridge are learned jointly, resulting in a robust embedding space for normal samples. Moreover, to enhance generalization across unseen anomaly domains, we introduce a dispersion feature learning mechanism that maps intermediate features to a hyperspherical space, leveraging a mixture of von Mises-Fisher (vMF) distributions. This approach bolsters directional feature extraction and promotes robust inter-sample separation, facilitating effective identification of out-of-distribution samples. Experiments demonstrate that our method greatly improves detection capabilities for unseen anomalies. In the single-anomaly training setting, DPDL outperforms the next best-performing method by over 8.3% on datasets including AITEX, ELPV, and Mastcam.

In summary, our contributions are three-fold: i) we propose a distribution prototype diffusion learning framework that jointly learns multiple Gaussian prototypes and the associated diffusion bridge, creating a compact and discriminative embedding space; ii) we develop dispersion feature learning in hyperspherical space to enhance inter-sample

separation and improve generalization; iii) we achieve state-of-the-art performance in 9 public datasets, demonstrating the efficacy of our approach.

2. Related Work

Open-set Supervised Anomaly Detection. Open-set supervised anomaly detection (OSAD) seeks to develop a robust anomaly detection framework that generalizes from a limited set of training anomalies to effectively identify previously unseen anomalies within an open-set context [1, 27, 34, 41, 46]. Leveraging the prior knowledge provided by observed anomalies, contemporary OSAD methods significantly mitigate false positive errors, thereby enhancing overall detection performance [9, 45]. Recently, DRA [9] learns disentangled representations of observed, pseudo, and residual anomalies to boost the detection of both seen and unseen anomalies. In contrast, AHL [45] simulates diverse heterogeneous anomaly distributions and employs collaborative differentiable learning, significantly improving the model’s generalization capacity.

Schrödinger Bridge. Schrödinger bridge (SB), widely recognized as the entropy-regularized optimal transport (OT) problem, involves learning a stochastic process that evolves from an initial probability distribution to a terminal distribution under the influence of a reference measure [5, 7, 16, 18, 23, 24, 37]. I²-SB [25] and UNSB [14] learn a nonlinear diffusion process between two given distributions or represent the SB problem as a series of adversarial learning problems to realize the image transformation task. Recently, LightSB [10, 17] introduces a novel, fast, and simple SB solver, which achieves optimal matching in practice through the Gaussian mixture parameterization of the adjusted schrödinger potential.

3. Preliminaries

We focus on how to build the connection between two distributions p_0 and p_1 , where the distributions are defined as absolutely continuous Borel probability distributions with finite second-order moments. Building upon the foundation of entropy-regularized optimal transport (EOT) [5, 7, 16, 18, 23, 24, 32, 37], we review the related properties of EOT and the schrödinger bridge (SB) problem with a Wiener prior.

Entropy-regularized optimal transport (EOT). Given two point sets \mathcal{Z}_0 and \mathcal{Z}_1 , we seek for the optimal transport cost between any two points $z_0 \in \mathcal{Z}_0$ and $z_1 \in \mathcal{Z}_1$. This task may be formulated as an EOT problem with a parameter $\epsilon > 0$, *i.e.*, minimizing the following objective:

$$\min_{\pi \in \Pi(p_0, p_1)} \left\{ \int_{\mathbb{R}^D} \int_{\mathbb{R}^D} \frac{1}{2} \|z_0 - z_1\|^2 \pi(z_0, z_1) dz_0 dz_1 + \epsilon \text{KL}(z \parallel p_0 \times p_1) \right\}, \quad (1)$$

where $\Pi(p_0, p_1)$ denotes the set of transport plans, *i.e.*, joint probability distributions on $\mathbb{R}^D \times \mathbb{R}^D$ with marginals p_0 and p_1 , respectively, and KL denotes Kullback-Leibler divergence. The minimizer π^* of Eqn. (1) is guaranteed to exist, be unique, and absolutely continuous, and is referred as the EOT plan.

Schrödinger Bridge (SB). We define Ω as the space of \mathbb{R}^D -valued functions over time $t \in [0, 1]$, representing trajectories in \mathbb{R}^D that start at $t = 0$ and end at $t = 1$. We denote the set of probability distributions over Ω , *i.e.*, stochastic processes, by $\mathcal{P}(\Omega)$. The differential of the standard Wiener process is represented by dW_t . For a process $T \in \mathcal{P}(\Omega)$, we denote its joint distribution at $t = 0, 1$ by $\pi_T \in \mathcal{P}(\mathbb{R}^D \times \mathbb{R}^D)$. Similarly, we use $T|_{z_0, z_1}$ to denote the distribution of T for $t \in (0, 1)$, conditioned on T 's values z_0 and z_1 at $t = 0$ and $t = 1$, respectively.

Let $W^\epsilon \in \mathcal{P}(\Omega)$ represents a Wiener process with volatility $\epsilon > 0$, starting from p_0 at $t = 0$. Its differential is governed by the stochastic differential equation (SDE): $dW_t^\epsilon = \sqrt{\epsilon} dW_t$. The Schrödinger bridge problem with the Wiener prior W^ϵ between p_0 and p_1 is minimizing:

$$\min_{T \in \mathcal{F}(p_0, p_1)} \text{KL}(T \parallel W^\epsilon), \quad (2)$$

where $\mathcal{F}(p_0, p_1) \subset \mathcal{P}(\Omega)$ denotes the subset of stochastic processes that begin with distribution p_0 at $t = 0$ and reach p_1 at $t = 1$. This problem has a unique solution, a SDE diffusion process T^* defined: $dZ_t = g^*(Z_t, t) dt + dW_t^\epsilon$. The process T^* is referred to as SB, and $g^* : \mathbb{R}^D \times [0, 1] \rightarrow \mathbb{R}^D$ is the optimal drift.

Characterization of solutions. The EOT plan $\pi^* = \pi^{T^*}$ takes a specific form [18]:

$$\pi^*(z_0, z_1) = u^*(z_0) \exp\left(\frac{-\|z_0 - z_1\|^2}{2\epsilon}\right) v^*(z_1), \quad (3)$$

where $u^*, v^* : \mathbb{R} \rightarrow \mathbb{R}_+$ are measurable functions known as Schrödinger potentials. The optimal drift g^* is derived as:

$$g^*(z, t) = \epsilon \nabla_z \log \int_{\mathbb{R}^D} \mathcal{N}(z'|z, (1-t)\epsilon I_D) v^*(z') dz', \quad (4)$$

4. Method

4.1. Problem Formulation

Let $\mathcal{X}_{\text{tr}} = \{(x_i, y_i)\}$ denotes a weakly-supervised training set with only image-level labels, where x_i denotes one RGB image and $y_i \in \{0, 1\}$ denotes whether x_i is an anomaly sample (anomaly: $y_i = 1$, normal: $y_i = 0$). Hereby, \mathcal{X}_{tr} is consist of a normal subset $\mathcal{X}_{\text{tr}}^n$ ($|\mathcal{X}_{\text{tr}}^n| = N$) and an anomaly subset $\mathcal{X}_{\text{tr}}^a$ ($|\mathcal{X}_{\text{tr}}^a| = M$), formally, $\mathcal{X}_{\text{tr}} \doteq \mathcal{X}_{\text{tr}}^n \cup \mathcal{X}_{\text{tr}}^a$, where generally $N \gg M$. Given a testing set \mathcal{X}_{te} , we need to predict whether one sample $x \in \mathcal{X}_{\text{te}}$ is anomaly or normal. In OSAD, the anomaly patterns of the testing set do less recurred in those encountered training set. In

other word, the distribution of anomalies are obviously discrepant, *i.e.*, $P(\mathcal{X}_{\text{te}}^a) \neq P(\mathcal{X}_{\text{tr}}^a)$. Hereby, we need to learn a robust anomaly detection model ψ from the training set \mathcal{X}_{tr} , so that ψ accurately infers anomaly scores for test samples.

Our abstract idea is to learn latent distribution prototypes that not only encapsulate normal samples in a concise manner but also discriminate against anomaly samples. Given the abundance of observed normal samples, one natural approach is to characterize the distribution $P(\mathcal{X}_{\text{tr}}^n)$, where samples outside this distribution, $x \notin P(\mathcal{X}_{\text{tr}}^n)$, would be awarded higher probabilities as anomalies. Considering the inherent diversity of normal samples, we endeavor to learn multiple simple distributions (*e.g.*, Gaussians) as prototypes \mathcal{P}_{MGP} , named multi-Gaussian prototypes (MGP). To embed input data into the prototype space, we introduce a generative bridge model ψ_p for distribution transformation. The more *abstract* formulation is given as follows:

$$\min_{\psi_p, \mathcal{P}_{\text{MGP}}, f} D_p(\psi_p(\mathcal{F}_{\text{tr}}^n), \psi_p(\mathcal{F}_{\text{tr}}^a), \mathcal{P}_{\text{MGP}}) + \lambda D_s(\mathcal{F}_{\text{tr}}^n, \mathcal{F}_{\text{tr}}^a), \quad (5)$$

$$\text{s.t.}, \psi_p : \mathcal{P}(\mathcal{F}) \xrightarrow{\text{bridge}} \mathcal{P}_{\text{MGP}}, \quad (6)$$

$$f : \mathcal{X} \xrightarrow{\text{feature}} \mathcal{F}, \quad (7)$$

where \mathcal{P}_{MGP} denotes the distribution prototypes to be learned, ψ_p is the flow function across probability distributions, D_p signifies the discriminative function in the space of prototypes, f stands for the feature extraction process, and D_s acts as a regularizer to increase feature discriminability. In the above formulation, besides distribution prototype learning (DPL), we also introduce dispersion feature learning (DFL) executed within a hyperspherical embedding space, *i.e.*, $D_s(\mathcal{F}_{\text{tr}}^n, \mathcal{F}_{\text{tr}}^a)$. The advantage of DFL is to prevent abrupt feature collapse in feature learning, thus preserving discriminative qualities. *The overview of our framework* is abstractly depicted in Fig. 1. Detailed elaboration¹ on these aspects will be provided in the subsequent sections.

4.2. Distribution Prototype Learning

Distribution prototype learning is operated in the feature space. Hence, to extract intermediate image features, we can leverage those classic networks as the backbone, such as ResNet-18. Formally, the feature extraction process, denoted as a function $f : \mathcal{X} \rightarrow \mathcal{F}$, transforms an image x into the intermediate feature $\mathbf{x} = f(x)^2 \in \mathbb{R}^d$. Consequently, we designate the intermediate feature sets of normal and anomaly samples as $\mathcal{F}_{\text{tr}}^n = \{\mathbf{x}_i^n | i = 1, \dots, N\}$ and $\mathcal{F}_{\text{tr}}^a = \{\mathbf{x}_i^a | i = 1, \dots, M\}$, respectively.

Considering the rarity of anomalies and the diversity of normal samples, it is pertinent to capture the intricate distributions of normal samples by mapping the distribution

¹The concrete algorithm is deferred to the supplementary material.

²Here a flatten operation is used on convolution maps for vectorization.

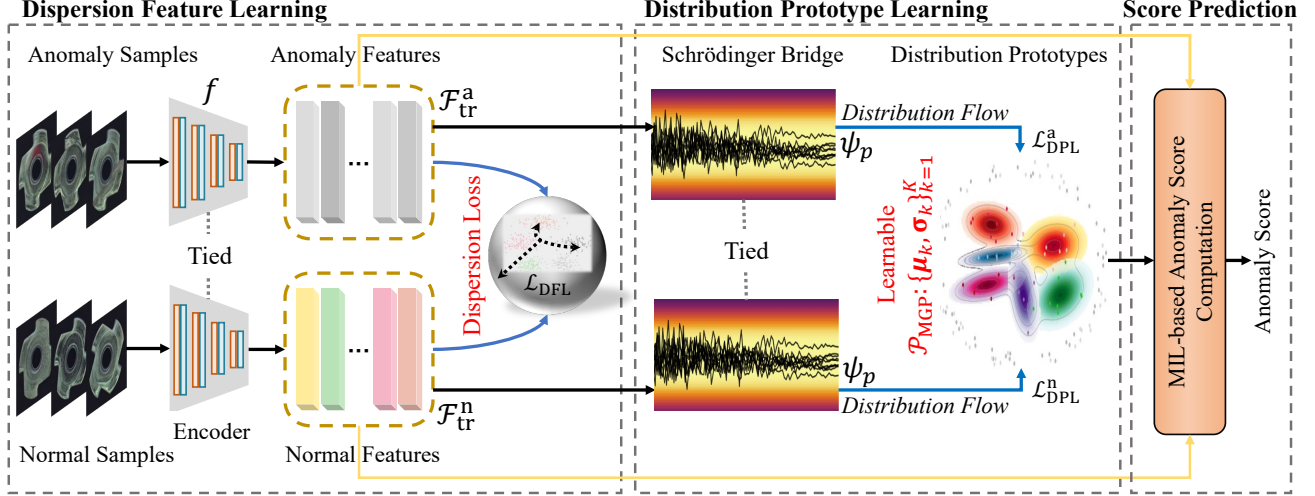


Figure 1. Our proposed DPDL framework. It comprises three distinct modules: Distribution Prototype Learning (DPL, Sec. 4.2), Dispersion Feature Learning (DFL, Sec. 4.3), and anomaly score prediction (Sec. 4.4). DPL transforms the distribution of normal samples to a space of learnable multiple Gaussian prototypes through building schrödinger bridge, meantime pushing anomaly distribution away from these prototypes. DFL operates in a hyperspherical space, enlarging the distances of intermediate features of all samples in a hyperspherical space to strengthen feature generalization for detecting anomalies. The score prediction module leverages a multi-instance-learning method to compute anomaly scores.

$p_0 = P(\mathcal{F}_{tr}^n)$ of intermediate features to a distinct and well-characterized distribution p_1 like Gaussian. But due to various normal samples, we opt for a multi-Gaussian prototypes (MGP) comprising multiple Gaussian distributions as prototypes $\mathcal{P}_{MGP} = \{\mathcal{P}_i \doteq \mathcal{N}(\boldsymbol{\mu}_i, \boldsymbol{\sigma}_i) | i = 1, \dots, C\}$. Given a normal sample \mathbf{x}_i^n , we expect to align it with the closest prototype with high likelihood. However, in the open-set setting, it is challenge to transform unseen points $\mathbf{x} \sim p_0$ to the target distribution p_1 . Drawing inspiration from the capability of diffusion generation models in aligning disparate distributions, we frame the transition from source domain distribution p_0 to target domain distribution p_1 as a Schrödinger bridge problem. As formulated in Eqn. (6), we need learn an essential bridge flow $\psi_p : P(\mathcal{F}_{tr}^n) \xrightarrow{\text{bridge}} \mathcal{P}_{MGP}$. After bridge transformation, the condition probability in optimal transport plan conforms to:

$$\pi(\psi_p(\mathbf{x})|\mathbf{x}) \propto \underbrace{\sum_{c=1}^C \alpha_c \mathcal{N}(\psi_p(\mathbf{x}); \boldsymbol{\mu}_c, \boldsymbol{\sigma}_c)}_{\doteq \phi_1(\psi_p(\mathbf{x}))}, \quad (8)$$

where the parameters $\{\alpha_c, \boldsymbol{\mu}_c, \boldsymbol{\sigma}_c\}_{c=1}^C$ (known as Gaussian mixed model (GMM), abstracted into the function ϕ_1) as well as the flow function ψ_p (in bridge) need to be learned. For simplicity, below we adopt diagonal matrices for $\boldsymbol{\sigma}_c$.

Drawing inspiration from previous works [10, 17], we reframe distribution prototype learning in Eqn. (8) as the Schrödinger bridge. Given the specific form taken by the EOT plan described in Eqn. (3), we redefine these measurable functions $u, v : \mathbb{R} \rightarrow \mathbb{R}_+$, termed Schrödinger poten-

tials, as follows:

$$u(\mathbf{x}_i^n) \doteq \exp\left(\frac{\|\mathbf{x}_i^n\|^2}{2\epsilon}\right) \phi_0(\mathbf{x}_i^n), \quad (9)$$

$$v(\psi(\mathbf{x}_i^n)) \doteq \exp\left(\frac{\|\psi(\mathbf{x}_i^n)\|^2}{2\epsilon}\right) \phi_1(\psi(\mathbf{x}_i^n)), \quad (10)$$

where ϕ_0 is defined within the source feature domain \mathcal{F}_{tr} , and ϕ_1 is defined in Eqn. (8). ϵ is set to 0.001 in our experiments. Accordingly, Eqn. (3) can be converted to:

$$\pi(\mathbf{x}_i^n, \psi(\mathbf{x}_i^n)) = \phi_0(\mathbf{x}_i^n) \exp\left(\frac{\langle \mathbf{x}_i^n, \psi(\mathbf{x}_i^n) \rangle}{\epsilon}\right) \phi_1(\psi(\mathbf{x}_i^n)), \quad (11)$$

Hence, the condition probability of the transport plan in Eqn. (8) could be exactly defined as

$$\pi(\psi(\mathbf{x}_i^n)|\mathbf{x}_i^n) \doteq \eta(\mathbf{x}_i^n, \psi(\mathbf{x}_i^n)) \phi_1(\psi(\mathbf{x}_i^n)), \quad (12)$$

where the connection factor is denoted as $\eta(\mathbf{x}_i^n, \psi(\mathbf{x}_i^n)) = \frac{1}{\varpi(\mathbf{x}_i^n)} \exp\left(\frac{\langle \mathbf{x}_i^n, \psi(\mathbf{x}_i^n) \rangle}{\epsilon}\right)$ with the normalization term $\varpi(\mathbf{x}_i^n) = \int \exp(\langle \mathbf{x}_i^n, \psi(\mathbf{x}_i^n) \rangle) \phi_1(\psi(\mathbf{x}_i^n)) d\psi(\mathbf{x}_i^n)$. According to Eqns. (8) and (12), we can further derive a more tractable form:

$$\pi(\psi(\mathbf{x}_i^n)|\mathbf{x}_i^n) = \tilde{\eta}(\mathbf{x}_i^n) \sum_{c=1}^C \tilde{\alpha}_c(\mathbf{x}_i^n) \mathcal{N}(\psi(\mathbf{x}_i^n); \tilde{\boldsymbol{\mu}}_c(\mathbf{x}_i^n), \boldsymbol{\sigma}_c), \quad (13)$$

where the normalization factor is denoted as $\tilde{\eta}(\mathbf{x}_i^n) = 1 / \sum_{c=1}^C \tilde{\alpha}_c(\mathbf{x}_i^n)$, the coefficients of multi-Gaussian are defined as $\tilde{\alpha}_c(\mathbf{x}_i^n) = \alpha_c \exp\left(\frac{1}{2}(\mathbf{x}_i^n)^\top \boldsymbol{\sigma}_c \mathbf{x}_i^n + \frac{1}{\epsilon}(\tilde{\boldsymbol{\mu}}_c)^\top(\mathbf{x}_i^n)\right)$, and the mean vectors are calculated as $\tilde{\boldsymbol{\mu}}_c(\mathbf{x}_i^n) = \boldsymbol{\mu}_c + \frac{1}{\epsilon} \boldsymbol{\sigma}_c \mathbf{x}_i^n$.

We proceed with deriving the bridge function ψ_p that represents a SDE process: $d\mathbf{x}_t = g(x_t, t)dt + \sqrt{\epsilon}dW_t$ where the shift function g is solved. According to Eqn. (4), we can obtain the shift function of diffusion process as follows:

$$g(\mathbf{x}_i^n, t) = \epsilon \rho_{\text{MGP}}(\mathbf{x}_i^n) \nabla_{\mathbf{x}_i^n} \log(\mathcal{N}(\mathbf{x}_i^n | 0, \epsilon(1-t)\mathbf{I})), \quad (14)$$

where the coefficients ρ_{MGP} defined on multiple distribution prototypes is calculated as: $\rho_{\text{MGP}}(\mathbf{x}_i^n) = \sum_{c=1}^C (\alpha_c \mathcal{N}(\tilde{\boldsymbol{\mu}}_c(\mathbf{x}_i^n) | \mathbf{0}, \boldsymbol{\sigma}_c) \mathcal{N}(h_c(\mathbf{x}_i^n, t) | 0, \boldsymbol{\Sigma}_c^t))$, with another Gaussian of $h_c(\mathbf{x}_i^n, t) = \frac{1}{\epsilon(1-t)} \mathbf{x}_i^n + \boldsymbol{\sigma}_c^{-1} \tilde{\boldsymbol{\mu}}_c(\mathbf{x}_i^n)$ and $\boldsymbol{\Sigma}_c^t = \frac{t}{\epsilon(1-t)} \mathbf{I} + \boldsymbol{\sigma}_c^{-1}$. *The derivation about Eqns. (13) and (14) is deferred to the supplementary material.*

Distribution prototypes initialization. Jointly learning prototypes $\{\alpha_c, \boldsymbol{\mu}_c, \boldsymbol{\sigma}_c\}_{c=1}^C$ and the bridge transformation ψ_p (also the shift g) is a challenging task as they are interdependent. For this, we leverage a vector quantization function to learn a codebook \mathcal{E} of prototypes within a discrete latent space from training data. Specifically, given an input image feature \mathbf{x}_i^n , we can assign \mathbf{x}_i^n to the closest prototype \mathbf{e}_k by minimizing the L2 distance between \mathbf{x}_i^n and each of prototypes $\mathbf{e}_c \in \mathcal{E}$, as follows:

$$\min_{\{\mathbf{e}_c\}} \mathbb{E}_{\mathbf{x}_i^n \in \mathcal{F}_{\text{tr}}} [\|\mathbf{x}_i^n - \mathbf{e}_{c^*}\|_2^2], \text{ s.t. } , c^* = \arg \min_c \|\mathbf{x}_i^n - \mathbf{e}_c\|_2, \quad (15)$$

where c^* denotes the index of the prototype closest to \mathbf{x}_i^n . The learned $\{\mathbf{e}_c\}_{c=1}^C$ are used to initialize the mean vectors $\{\boldsymbol{\mu}_c\}_{c=1}^C$, while the variances of all prototypes are set to the identity matrix. We observe that this initialization strategy accelerates the training process.

Distribution loss of normal and anomaly samples. As p_0 and p_1 are accessible only via samples \mathcal{F}_{tr} and prototypes \mathcal{P}_{MGP} , we optimize the empirical form in Eqn. (2) for normal samples as follows:

$$\mathcal{L}_{\text{DPL}}^n = \frac{1}{N} \sum_{i=1}^N \log \varpi_{\theta}(\mathbf{x}_i^n) - \frac{1}{C} \sum_{c=1}^C \log \phi_1(\boldsymbol{\mu}_c), \quad (16)$$

In contrast, for anomaly samples, we aim to push anomaly distribution away from p_1 , *i.e.*, negative loss, formally,

$$\mathcal{L}_{\text{DPL}}^a = \frac{1}{C} \sum_{c=1}^C \log \phi_1(\boldsymbol{\mu}_c) - \frac{1}{M} \sum_{i=1}^M \log \varpi_{\theta}(\mathbf{x}_i^a), \quad (17)$$

4.3. Dispersion Feature Learning

A critical challenge in OSAD is detecting previously unseen anomalies in open-set environments. Due to the limited anomaly observations, existing methods often use pseudo-anomaly generation strategies as a means of effective data augmentation. Nonetheless, the effectiveness of these methods heavily depends on the quality of the pseudo-anomaly feature embeddings. Notably, pseudo-anomaly distributions often inherit biases from the in-distribution

data, which differ from the unknown anomaly distributions in out-of-distribution data. Current methods fail to address the relationship between observed and unknown anomalies, particularly for out-of-distribution generalization.

To improve out-of-distribution detection, it is essential to promote a larger inter-sample dispersion, as greater distances among in-distribution samples facilitate their more effective separation from out-of-distribution samples. In other words, if all inter-sample distances are close to zero, *i.e.*, collapse to a single point, it becomes impossible to differentiate between samples. Hence, promoting separability through a larger inter-sample dispersion is critical for accurately identifying samples that do not belong to known categories. To do so, we map the features into a *hyperspherical* space. Draws inspiration from the vMF distribution [30] in directional statistics, we compute spherical Gaussian distributions for unit-norm features $\hat{\mathbf{x}}_i = \mathbf{x}_i / \|\mathbf{x}_i\|_2$. The probability density function of a unit vector $\hat{\mathbf{x}}_i \in \mathbb{R}^D$ is defined in the *hyperspherical* space as follows:

$$p_D(\hat{\mathbf{x}}_i; \hat{\mathbf{x}}_j, \kappa) = F_D(\kappa) \exp(\kappa \langle \hat{\mathbf{x}}_i, \hat{\mathbf{x}}_j \rangle), \quad (18)$$

where $\kappa \geq 0$ controls the concentration of the distribution around the mean direction $\hat{\mathbf{x}}_j$ and $F_D(\kappa)$ is the normalization factor. A larger κ value increases concentration around the mean, while in the extreme case $\kappa = 0$, sample points are uniformly distributed on the hypersphere. Therefore, we design a dispersion loss to optimize large angular distances between the features of all samples:

$$\mathcal{L}_{\text{DFL}} = \frac{1}{U} \sum_{i=1}^U \log \frac{1}{U-1} \sum_{i,j=1}^U \mathbb{1}\{i \neq j\} \exp(\kappa \langle \hat{\mathbf{x}}_i, \hat{\mathbf{x}}_j \rangle), \quad (19)$$

where $U = N + M$, and κ is set to 10 in our experiments.

4.4. Anomaly Score Prediction

Based on the above designs, we leverage the multiple-instance-learning (MIL)-based method proposed in [34] to effectively learn anomaly scores. Similar to the work [9], we design three modules $M = \{M_a, M_n \text{ and } M_r\}$ for estimating anomaly scores. Firstly, for the feature map \mathbf{x}_i^3 , we generate pixel-wise feature vectors $\mathcal{V} = \{\mathbf{v}_i\}_{i=1}^{H' \times W'}$ to represent the feature of small patches of the image \mathbf{x}_i , where (H', W') denotes the size of the feature map. These pixel-wise representations are then mapped by an anomaly classifier S_a to estimate pixel-level anomaly scores. To capture those points with the most salient anomalies, we compute the top- K most anomaly pixel points and define the loss function as:

$$\mathcal{L}_{M_a}(\mathbf{x}_i, y_i) = \mathcal{L}_{\text{binary}}\left(\frac{1}{K} \sum \text{Top}_K\{S_a(\mathbf{v}_i; \theta_a)\}, y_i\right), \quad (20)$$

³Here \mathbf{x}_i refers to convolution maps without flattening (as used above).

where $\mathcal{L}_{\text{binary}}$ refers to a binary classification loss function, and Top_K selects the highest K anomaly scores among all the vectors. Secondly, we use M_n to learn the normal features:

$$\mathcal{L}_{M_n}(\mathbf{x}_i, y_i) = \mathcal{L}_{\text{binary}}(S_n(\frac{1}{H' \times W'} \sum_{i=1}^{H' \times W'} \mathbf{v}_i; \theta_n), y_i), \quad (21)$$

where $S_n : \mathcal{V} \rightarrow \mathbb{R}$ is a fully connected binary anomaly classifier. Finally, we define M_r to compute the residual anomaly scores between fine-grained visual semantics and abstract prototypes:

$$\mathcal{L}_{M_r} = \mathcal{L}_{\text{binary}}(S_r((\psi_p(\mathbf{x}_i) - \boldsymbol{\mu}_{c^*})/\boldsymbol{\sigma}_{c^*}; \theta_r), y_i), \quad (22)$$

where c^* denotes the index of the most probable prototypes, *i.e.*, $c^* = \arg \max_c \mathcal{N}(\psi_p(\mathbf{x}_i); \boldsymbol{\mu}_c, \boldsymbol{\sigma}_c)$, and S_r utilize the same method to obtain anomaly score as S_a .

Training. During the training phase, the SB and three prediction modules are jointly trained. To this end, we employ an objective function that encompasses three components as follows:

$$\mathcal{L} = \underbrace{\mathcal{L}_{M_a} + \mathcal{L}_{M_n} + \mathcal{L}_{M_r}}_{\text{MIL-based learning}} + \underbrace{\mathcal{L}_{\text{DPL}}^n + \mathcal{L}_{\text{DPL}}^a}_{\text{SB transform}} + \underbrace{\lambda \mathcal{L}_{\text{DFL}}}_{\text{dispersion}}. \quad (23)$$

where the coefficient λ modulates the relative importance of dispersion loss, and the learnable parameters include $\{\alpha_c, \boldsymbol{\mu}_c, \boldsymbol{\sigma}_c\}$, θ_{ψ_p} , and $\{\theta_a, \theta_n, \theta_r\}$.

Inference. During the test phase, we find the most similar class prototype through SB, and subsequently compute the anomaly score by adding the scores from both S_a and S_r , while subtracting the normal score obtained from S_n for the given test image.

In summary, we reduce all the above processes into an algorithm given in the supplementary material for clarity.

5. Experiment

5.1. Dataset and Evaluation Metric

Dataset To validate the effectiveness of DPDL, comprehensive experiments are conducted on nine real-world AD datasets, including six industrial defect detection datasets (MVTec AD [3], Optical [40], SDD [?], AITEX [38], ELPV [8], Mastcam [13]) and three medical image datasets (Hyper-Kvasir [4], Brain-MRI [36], HeadCT [36]). We follow the previous OSAD baselines [9, 45] to adopt two protocols for sampling, including general setting and hard setting. The general setting assumes that anomaly examples are randomly sampled from the anomaly class, while the hard setting samples from a single class to assess generalization to new or unseen anomaly classes.

Evaluation Metric We utilize the widely adopted Area Under ROC Curve (AUC) as a metric to evaluate the performance across all methods and settings. All reported AUCs are averaged results over five independent runs.

5.2. Baselines

We compare DPDL against six related state-of-the-art OSAD baselines, including SAOE [19, 31, 39], MLEP [27], FLOS [35], DevNet [34], DRA [9], and AHL [45]. MLEP, DevNet, DRA, and AHL are specifically designed for OSAD. SAOE is a supervised detector enhanced with synthetic anomalies and anomaly exposure, whereas FLOS is an imbalanced classifier leveraging focal loss.

5.3. Implementation Details

The input image size is $448 \times 448 \times 3$. We set K in the top- K MIL to 10% of the number of all scores per score map. AdamW optimizer [29] is used for the parameter optimization using an initial learning rate 2×10^{-4} with a weight decay of 1×10^{-5} . DPDL is trained on one NVIDIA GeForce RTX 4090 GPU, which are trained using 50 epochs, with 20 iterations per epoch. Following previous protocol [9, 45], we evaluate performance with anomaly sample numbers of $M = 10$ and $M = 1$, and for robust detection of unseen anomalies, we use CutMix [43] to create pseudo-anomaly samples as augmented data for known anomalies. The prototype quantity C is set to 32 as default. Our code will be available at our site⁴.

5.4. Results under General Setting

Tab. 1 highlights DPDL’s strong performance. In the challenging scenario of single-anomaly detection, DPDL improves the performance of AHL [45] by more than 8.3% on the AITEX, ELPV, and Mastcam datasets. Furthermore, it achieves significant improvements across six additional datasets, which suggest the effective utilization of few-shot anomaly examples in DPDL, while mitigating overfitting to the seen anomalies. When shifting to ten anomaly examples settings, DPDL continues to maintain a significant lead with over 5.4% improvement on those datasets. Given the rich and diverse set of normal samples in these datasets, DPDL leverages the DPL component to encapsulate these samples within a compact, discriminative distribution space, while effectively pushing anomalous samples outside this space, thereby enabling accurate anomaly detection. In the setting with ten abnormal samples, although existing methods have reached performance saturation on the MVTecAD, Optical, and SDD datasets, DPDL still has a certain lead, demonstrating the strong ability of DPL and DFL in learning tight boundaries of normal sample distributions and generalizing to previously unseen anomaly domains. Furthermore, when evaluated on the medical datasets BrainMRI and HeadCT, DPDL demonstrates competitive performance despite these datasets being notably small in scale and containing only a single class. This highlights the algorithm’s ability to deliver robust results even in data-scarce conditions.

⁴<https://github.com/fuyunwang/DPDL>

Table 1. AUC performance (mean \pm std) across nine real-world AD datasets is reported under the general setting. **red** highlights the best results, and **blue** indicates sub-optimal outcomes. All baseline SOTA results are sourced from the original papers [9, 45].

Dataset	DevNet	FLOS	SAOE	MLEP	DRA	AHL	DPDL (Ours)
Ten Training Anomaly Examples							
MVTec AD	0.945 \pm 0.004	0.939 \pm 0.007	0.926 \pm 0.010	0.907 \pm 0.005	0.959 \pm 0.003	0.970 \pm 0.002	0.977 \pm 0.002
Optical	0.782 \pm 0.065	0.720 \pm 0.055	0.941 \pm 0.013	0.740 \pm 0.039	0.965 \pm 0.006	0.976 \pm 0.004	0.983 \pm 0.005
SDD	0.988 \pm 0.006	0.967 \pm 0.018	0.955 \pm 0.020	0.983 \pm 0.013	0.991 \pm 0.005	0.991 \pm 0.001	0.996 \pm 0.001
AITEX	0.887 \pm 0.013	0.841 \pm 0.049	0.874 \pm 0.024	0.867 \pm 0.037	0.893 \pm 0.017	0.925 \pm 0.013	0.975 \pm 0.007
ELPV	0.846 \pm 0.022	0.818 \pm 0.032	0.793 \pm 0.047	0.794 \pm 0.047	0.845 \pm 0.013	0.850 \pm 0.004	0.937 \pm 0.003
Mastcam	0.790 \pm 0.021	0.703 \pm 0.029	0.810 \pm 0.029	0.798 \pm 0.026	0.848 \pm 0.008	0.855 \pm 0.005	0.934 \pm 0.010
Hyper-Kvasir	0.829 \pm 0.018	0.773 \pm 0.029	0.666 \pm 0.050	0.600 \pm 0.069	0.834 \pm 0.004	0.880 \pm 0.003	0.939 \pm 0.005
BrainMRI	0.958 \pm 0.012	0.955 \pm 0.011	0.900 \pm 0.041	0.959 \pm 0.011	0.970 \pm 0.003	0.977 \pm 0.001	0.969 \pm 0.005
HeadCT	0.982 \pm 0.009	0.971 \pm 0.004	0.935 \pm 0.021	0.972 \pm 0.014	0.972 \pm 0.002	0.999 \pm 0.003	0.981 \pm 0.003
One Training Anomaly Example							
MVTec AD	0.780 \pm 0.020	0.755 \pm 0.136	0.834 \pm 0.007	0.744 \pm 0.019	0.883 \pm 0.008	0.901 \pm 0.003	0.927 \pm 0.002
Optical	0.523 \pm 0.003	0.518 \pm 0.003	0.815 \pm 0.014	0.516 \pm 0.009	0.888 \pm 0.012	0.888 \pm 0.007	0.915 \pm 0.002
SDD	0.881 \pm 0.009	0.840 \pm 0.043	0.781 \pm 0.009	0.811 \pm 0.045	0.859 \pm 0.014	0.909 \pm 0.001	0.917 \pm 0.003
AITEX	0.598 \pm 0.070	0.538 \pm 0.073	0.675 \pm 0.094	0.564 \pm 0.055	0.692 \pm 0.124	0.734 \pm 0.008	0.838 \pm 0.008
ELPV	0.514 \pm 0.076	0.457 \pm 0.056	0.635 \pm 0.092	0.578 \pm 0.062	0.675 \pm 0.024	0.828 \pm 0.005	0.897 \pm 0.002
Mastcam	0.595 \pm 0.016	0.542 \pm 0.017	0.662 \pm 0.018	0.625 \pm 0.045	0.692 \pm 0.058	0.743 \pm 0.003	0.838 \pm 0.011
Hyper-Kvasir	0.653 \pm 0.037	0.668 \pm 0.004	0.498 \pm 0.100	0.445 \pm 0.040	0.690 \pm 0.017	0.768 \pm 0.015	0.821 \pm 0.007
BrainMRI	0.694 \pm 0.004	0.693 \pm 0.036	0.531 \pm 0.060	0.632 \pm 0.017	0.744 \pm 0.004	0.866 \pm 0.004	0.893 \pm 0.004
HeadCT	0.742 \pm 0.076	0.698 \pm 0.092	0.597 \pm 0.022	0.758 \pm 0.038	0.796 \pm 0.105	0.825 \pm 0.014	0.865 \pm 0.005

Table 2. AUC results (mean \pm std) under the hard setting. The best and second-best results are highlighted in **red** and **blue**, respectively. Carpet and Metal_nut are subsets of MVTec AD. The datasets used are consistent with those in [9, 45], where those datasets only containing one anomaly class are excluded to adapt for the hard setting. For detailed class-level results, please refer to the supplementary materia.

Dataset	DevNet	FLOS	SAOE	MLEP	DRA	AHL	DPDL (Ours)
Ten Training Anomaly Examples							
Carpet (mean)	0.847 \pm 0.017	0.761 \pm 0.012	0.762 \pm 0.073	0.751 \pm 0.023	0.935 \pm 0.013	0.949 \pm 0.002	0.956 \pm 0.004
Metal_nut (mean)	0.965 \pm 0.011	0.922 \pm 0.014	0.855 \pm 0.016	0.878 \pm 0.058	0.945 \pm 0.017	0.972 \pm 0.002	0.978 \pm 0.002
AITEX (mean)	0.683 \pm 0.032	0.635 \pm 0.043	0.724 \pm 0.032	0.626 \pm 0.041	0.733 \pm 0.009	0.747 \pm 0.002	0.798 \pm 0.005
ELPV (mean)	0.702 \pm 0.023	0.642 \pm 0.032	0.683 \pm 0.047	0.745 \pm 0.020	0.766 \pm 0.029	0.788 \pm 0.003	0.818 \pm 0.003
Mastcam (mean)	0.588 \pm 0.011	0.616 \pm 0.021	0.697 \pm 0.014	0.588 \pm 0.016	0.695 \pm 0.004	0.721 \pm 0.003	0.778 \pm 0.007
Hyper-Kvasir (mean)	0.822 \pm 0.019	0.786 \pm 0.021	0.698 \pm 0.021	0.571 \pm 0.014	0.844 \pm 0.009	0.854 \pm 0.004	0.864 \pm 0.002
One Training Anomaly Example							
Carpet (mean)	0.767 \pm 0.018	0.678 \pm 0.040	0.753 \pm 0.055	0.679 \pm 0.029	0.901 \pm 0.006	0.932 \pm 0.003	0.941 \pm 0.006
Metal_nut (mean)	0.855 \pm 0.016	0.855 \pm 0.024	0.816 \pm 0.029	0.825 \pm 0.023	0.932 \pm 0.017	0.939 \pm 0.004	0.944 \pm 0.003
AITEX (mean)	0.646 \pm 0.034	0.624 \pm 0.024	0.674 \pm 0.034	0.466 \pm 0.030	0.684 \pm 0.033	0.707 \pm 0.007	0.753 \pm 0.005
ELPV (mean)	0.648 \pm 0.057	0.691 \pm 0.008	0.614 \pm 0.048	0.566 \pm 0.111	0.703 \pm 0.022	0.740 \pm 0.003	0.762 \pm 0.003
Mastcam (mean)	0.511 \pm 0.013	0.524 \pm 0.013	0.689 \pm 0.037	0.541 \pm 0.007	0.667 \pm 0.012	0.673 \pm 0.010	0.733 \pm 0.004
Hyper-Kvasir (mean)	0.595 \pm 0.023	0.571 \pm 0.004	0.406 \pm 0.018	0.480 \pm 0.044	0.700 \pm 0.009	0.706 \pm 0.007	0.715 \pm 0.004

5.5. Results under the Hard Setting

Tab. 2 summarizes the performance comparison under the hard setting. It is evident that DPDL achieves the highest AUC scores in both the single-anomaly and ten-anomaly sample settings. Specifically, compared to the closest competing method, AHL [45], DPDL achieves an improvement in AUC scores ranging from 0.6% to 7.9% in the ten anomaly examples settings and from 0.5% to 8.9% in the one anomaly example settings, respectively. The observed improvement can be attributed to the strong generalization

ability of DPDL in detecting unseen anomaly classes, even when the model is trained on only a single anomaly class.

5.6. Ablation Study

The ablation study in Fig. 2 highlights the critical roles of the DPL and DFL components in improving DPDL’s open-set anomaly detection. We denote the variants that remove only DPL or DFL as ‘DPDL w/o DPL’ and ‘DPDL w/o DFL’, respectively. Compared to the full DPDL model, removing neither DPL nor DFL leads to a significant AUC decline, illustrating their critical utility. Specifically, ‘DPDL

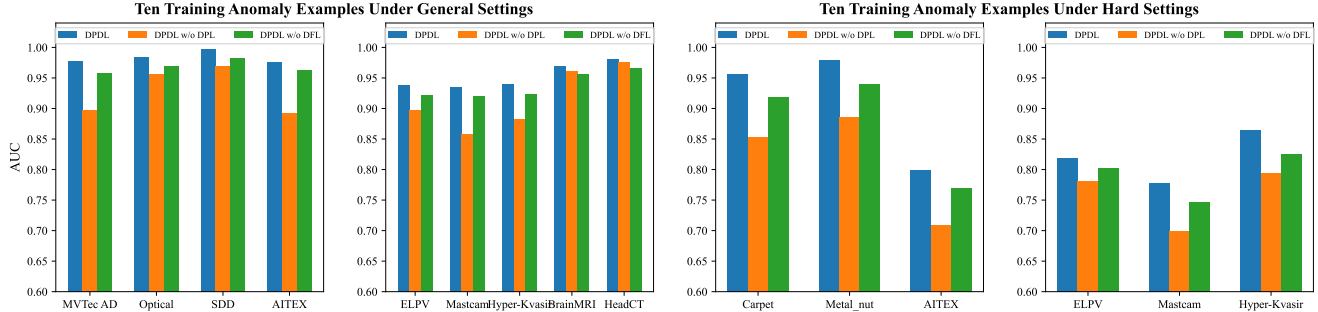


Figure 2. Ablation study for SB and DFL under the general settings and hard settings.

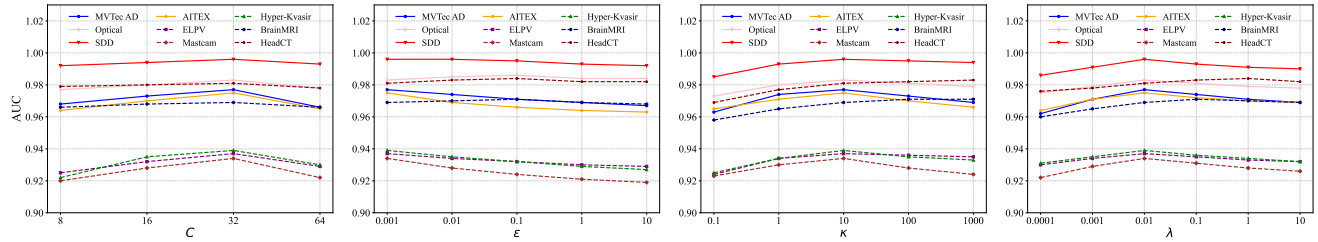


Figure 3. Parameter sensitivity analysis for C , ϵ , κ and λ .

Table 3. An ablation study for M_n , M_a and M_r .

M_n	M_a	M_r	AITEX	ELPV	Mastcam
Ten Training Anomaly Examples Under General Settings					
\times	\times	\checkmark	0.928 ± 0.019	0.914 ± 0.021	0.899 ± 0.036
\checkmark	\times	\checkmark	0.939 ± 0.023	0.919 ± 0.011	0.908 ± 0.017
\times	\checkmark	\checkmark	0.963 ± 0.008	0.930 ± 0.013	0.924 ± 0.019
\checkmark	\checkmark	\checkmark	0.975 ± 0.007	0.937 ± 0.003	0.934 ± 0.010
Ten Training Anomaly Examples Under Hard Settings					
\times	\times	\checkmark	0.746 ± 0.025	0.797 ± 0.026	0.723 ± 0.017
\checkmark	\times	\checkmark	0.758 ± 0.035	0.802 ± 0.024	0.736 ± 0.028
\times	\checkmark	\checkmark	0.781 ± 0.014	0.811 ± 0.018	0.762 ± 0.021
\checkmark	\checkmark	\checkmark	0.798 ± 0.005	0.818 ± 0.003	0.778 ± 0.007

w/o DPL’ exhibits the most significant performance drop on industrial anomaly datasets, reflecting DPL’s prominent role in learning precise and tight distribution boundaries for normal samples. By transforming normal samples into Gaussian distribution prototype space and pushing abnormal samples away, DPL enhances the recognition ability of anomaly samples. Meanwhile, ablation studies on ‘DPDL w/o DFL’ further highlight the critical role of the DFL component. By performing discreteness feature learning in hyperspherical space, DFL enhances the generalization ability to out-of-distribution anomalies.

Additionally, the ablation experiments on M_n , M_a , and M_r across three datasets in Tab. 3 reveal their varying contributions. DPDL shows the most significant performance drop when M_r is removed, which illustrates that M_r plays the most critical role in detecting anomalies. Furthermore, the removal of M_a and M_n lead to a noticeable performance

drop in DPDL, which underscores their essential roles.

5.7. Parameter Sensitivity Analysis

Fig. 3 illustrates the results of the four hyperparameters under the general settings across nine datasets. Overall, the performance remains stable within a certain range of hyperparameter variations, demonstrating the DPDL’s robustness. **Prototype quantity C .** We begin by investigating the critical impact of the number of initialized prototypes C on distributed prototype learning in DPDL. We select $\{8, 16, 32, 64\}$ as the values for the hyperparameters. As C increases, DPDL’s performance improves steadily, but excessively large values of C hinder the model’s effectiveness. This phenomenon is particularly pronounced on AITEX, Mastcam, MVTEcAD, and Hyper-Kvasir, which contain more categories. One possible explanation is that a prototype space with too few prototypes loses discriminative information, while an excessively large number of prototypes reduces the compactness of the space.

DPL trajectory ϵ in Eqns. (9), (10), (11) and (14). It can be observed that, particularly on the AITEX, Mastcam, and MVTEcAD datasets with a larger number of categories, DPDL exhibits a relatively stable performance decline as ϵ increases. As a crucial parameter in SB, ϵ governs the trajectory state. Since smaller values produce straighter trajectories and larger values increase fluctuation, smaller ϵ facilitates sampling more robust abstract prototypes from the relatively dispersed conditional distribution.

DFL tightness κ . According to Fig. 3, increasing κ generally enhances model performance, but values above $\kappa = 10$ introduce negative effects in certain scenarios. A possible reason is that excessive sample dispersion makes it more

challenging to tighten the normal distribution boundary.

Loss parameter λ . We conduct a sensitivity analysis on the loss parameters λ . It can be observed that setting $\lambda = 0.01$ achieves optimal performance on seven larger-scale datasets, while $\lambda = 1$ yields the best results on two datasets with limited data. As λ increases, the performance declines, potentially due to gradient conflicts among the dispersion loss, SB transform loss and the main task loss.

6. Conclusion

We propose Distribution Prototype Diffusion Learning (DPDL) for OSAD. DPDL leverages schrödinger bridge to map the normal distribution to a prototype space, simultaneously repelling anomalies to facilitate precise anomaly detection. We propose a dispersion feature learning way in hyperspherical space, which benefits the detection of out-of-distribution anomalies. Experimental results illustrate DPDL's robustness in diverse anomaly detection scenarios.

References

- [1] Andra Acsintoae, Andrei Florescu, Mariana-Iuliana Georgescu, Tudor Mare, Paul Sumedrea, Radu Tudor Ionescu, Fahad Shahbaz Khan, and Mubarak Shah. Ubnormal: New benchmark for supervised open-set video anomaly detection. In *Proceedings of the IEEE/CVF conference on computer vision and pattern recognition*, pages 20143–20153, 2022. 1, 2
- [2] Aimira Baitieva, David Hurych, Victor Besnier, and Olivier Bernard. Supervised anomaly detection for complex industrial images. In *Proceedings of the IEEE/CVF Conference on Computer Vision and Pattern Recognition*, pages 17754–17762, 2024. 1
- [3] Paul Bergmann, Michael Fauser, David Sattlegger, and Carsten Steger. Mvtec ad—a comprehensive real-world dataset for unsupervised anomaly detection. In *Proceedings of the IEEE/CVF conference on computer vision and pattern recognition*, pages 9592–9600, 2019. 6, 1
- [4] Hanna Borgli, Vajira Thambawita, Pia H Smedsrud, Steven Hicks, Debesh Jha, Sigrun L Eskeland, Kristin Ranheim Randel, Konstantin Pogorelov, Mathias Lux, Duc Tien Dang Nguyen, et al. Hyperkvasir, a comprehensive multi-class image and video dataset for gastrointestinal endoscopy. *Scientific data*, 7(1):283, 2020. 6, 1
- [5] Yongxin Chen, Tryphon T Georgiou, and Michele Pavon. On the relation between optimal transport and schrödinger bridges: A stochastic control viewpoint. *Journal of Optimization Theory and Applications*, 169:671–691, 2016. 2
- [6] Songmin Dai, Yifan Wu, Xiaoqiang Li, and Xiangyang Xue. Generating and reweighting dense contrastive patterns for unsupervised anomaly detection. In *Proceedings of the AAAI Conference on Artificial Intelligence*, pages 1454–1462, 2024. 1
- [7] Valentin De Bortoli, James Thornton, Jeremy Heng, and Arnaud Doucet. Diffusion schrödinger bridge with applications to score-based generative modeling. *Advances in Neural Information Processing Systems*, 34:17695–17709, 2021. 2
- [8] Sergiu Deitsch, Vincent Christlein, Stephan Berger, Claudia Buerhop-Lutz, Andreas Maier, Florian Gallwitz, and Christian Riess. Automatic classification of defective photovoltaic module cells in electroluminescence images. *Solar Energy*, 185:455–468, 2019. 6, 1
- [9] Choubao Ding, Guansong Pang, and Chunhua Shen. Catching both gray and black swans: Open-set supervised anomaly detection. In *Proceedings of the IEEE/CVF conference on computer vision and pattern recognition*, pages 7388–7398, 2022. 1, 2, 5, 6, 7
- [10] Nikita Gushchin, Sergei Kholkin, Evgeny Burnaev, and Alexander Korotin. Light and optimal schrödinger bridge matching. In *Forty-first International Conference on Machine Learning*, 2024. 2, 4
- [11] Liren He, Zhengkai Jiang, Jinlong Peng, Liang Liu, Qiang Du, Xiaobin Hu, Wenbing Zhu, Mingmin Chi, Yabiao Wang, and Chengjie Wang. Learning unified reference representation for unsupervised multi-class anomaly detection. *arXiv preprint arXiv:2403.11561*, 2024. 1
- [12] Teng Hu, Jiangning Zhang, Ran Yi, Yuzhen Du, Xu Chen, Liang Liu, Yabiao Wang, and Chengjie Wang. Anomalydiffusion: Few-shot anomaly image generation with diffusion model. In *Proceedings of the AAAI Conference on Artificial Intelligence*, pages 8526–8534, 2024. 1
- [13] Hannah R Kerner, Kiri L Wagstaff, Brian D Bue, Danika F Wellington, Samantha Jacob, Paul Horton, James F Bell, Chiman Kwan, and Heni Ben Amor. Comparison of novelty detection methods for multispectral images in rover-based planetary exploration missions. *Data Mining and Knowledge Discovery*, 34:1642–1675, 2020. 6, 1
- [14] Beomsu Kim, Gihyun Kwon, Kwanyoung Kim, and Jong Chul Ye. Unpaired image-to-image translation via neural schrödinger bridge. *arXiv preprint arXiv:2305.15086*, 2023. 2
- [15] Daehyun Kim, Sungyong Baik, and Tae Hyun Kim. Sanflow: Semantic-aware normalizing flow for anomaly detection. *Advances in Neural Information Processing Systems*, 36:75434–75454, 2023. 1
- [16] Hyunsu Kim, Jongmin Yoon, and Juho Lee. Fast ensembling with diffusion schrödinger bridge. *arXiv preprint arXiv:2404.15814*, 2024. 2
- [17] Alexander Korotin, Nikita Gushchin, and Evgeny Burnaev. Light schrödinger bridge. *arXiv preprint arXiv:2310.01174*, 2023. 2, 4
- [18] Christian Léonard. A survey of the schrödinger problem and some of its connections with optimal transport. *arXiv preprint arXiv:1308.0215*, 2013. 2, 3
- [19] Chun-Liang Li, Kihyuk Sohn, Jinsung Yoon, and Tomas Pfister. Cutpaste: Self-supervised learning for anomaly detection and localization. In *Proceedings of the IEEE/CVF conference on computer vision and pattern recognition*, pages 9664–9674, 2021. 1, 6
- [20] Hanxi Li, Jingqi Wu, Hao Chen, Mingwen Wang, and Chunhua Shen. Efficient anomaly detection with budget annotation using semi-supervised residual transformer. *arXiv preprint arXiv:2306.03492*, 2023. 1

- [21] Xiaofan Li, Zhizhong Zhang, Xin Tan, Chengwei Chen, Yanyun Qu, Yuan Xie, and Lizhuang Ma. Promptad: Learning prompts with only normal samples for few-shot anomaly detection. In *Proceedings of the IEEE/CVF Conference on Computer Vision and Pattern Recognition*, pages 16838–16848, 2024. 1
- [22] Jingyi Liao, Xun Xu, Manh Cuong Nguyen, Adam Goodge, and Chuan Sheng Foo. Coft-ad: Contrastive fine-tuning for few-shot anomaly detection. *IEEE Transactions on Image Processing*, 2024. 1
- [23] Guan-Horng Liu, Tianrong Chen, Oswin So, and Evangelos Theodorou. Deep generalized schrödinger bridge. *Advances in Neural Information Processing Systems*, 35:9374–9388, 2022. 2
- [24] Guan-Horng Liu, Yaron Lipman, Maximilian Nickel, Brian Karrer, Evangelos A Theodorou, and Ricky TQ Chen. Generalized schrödinger bridge matching. *arXiv preprint arXiv:2310.02233*, 2023. 2
- [25] Guan-Horng Liu, Arash Vahdat, De-An Huang, Evangelos A Theodorou, Weili Nie, and Anima Anandkumar. i^2 -sb: Image-to-image schrödinger bridge. *arXiv preprint arXiv:2302.05872*, 2023. 2
- [26] Jiaqi Liu, Kai Wu, Qiang Nie, Ying Chen, Bin-Bin Gao, Yong Liu, Jinbao Wang, Chengjie Wang, and Feng Zheng. Unsupervised continual anomaly detection with contrastively-learned prompt. In *Proceedings of the AAAI Conference on Artificial Intelligence*, pages 3639–3647, 2024. 1
- [27] Wen Liu, Weixin Luo, Zhengxin Li, Peilin Zhao, Shenghua Gao, et al. Margin learning embedded prediction for video anomaly detection with a few anomalies. In *IJCAI*, pages 023–3, 2019. 1, 2, 6
- [28] Xinyue Liu, Jianyuan Wang, Biao Leng, and Shuo Zhang. Dual-modeling decouple distillation for unsupervised anomaly detection. *arXiv preprint arXiv:2408.03888*, 2024. 1
- [29] I Loshchilov. Decoupled weight decay regularization. *arXiv preprint arXiv:1711.05101*, 2017. 6
- [30] Kanti V Mardia and Peter E Jupp. *Directional statistics*. John Wiley & Sons, 2009. 5
- [31] Amir Markovitz, Gilad Sharir, Itamar Friedman, Lih Zelnik-Manor, and Shai Avidan. Graph embedded pose clustering for anomaly detection. In *Proceedings of the IEEE/CVF Conference on Computer Vision and Pattern Recognition*, pages 10539–10547, 2020. 6
- [32] Maxence Noble, Valentin De Bortoli, Arnaud Doucet, and Alain Durmus. Tree-based diffusion schrödinger bridge with applications to wasserstein barycenters. *Advances in Neural Information Processing Systems*, 36, 2024. 2
- [33] Guansong Pang, Chunhua Shen, and Anton Van Den Hengel. Deep anomaly detection with deviation networks. In *Proceedings of the 25th ACM SIGKDD international conference on knowledge discovery & data mining*, pages 353–362, 2019. 1
- [34] Guansong Pang, Choubo Ding, Chunhua Shen, and Anton van den Hengel. Explainable deep few-shot anomaly detection with deviation networks. *arXiv preprint arXiv:2108.00462*, 2021. 2, 5, 6
- [35] T-YLPG Ross and GKHP Dollár. Focal loss for dense object detection. In *proceedings of the IEEE conference on computer vision and pattern recognition*, pages 2980–2988, 2017. 6
- [36] Mohammadreza Salehi, Niousha Sadjadi, Soroosh Baselizadeh, Mohammad H Rohban, and Hamid R Rabbiee. Multiresolution knowledge distillation for anomaly detection. In *Proceedings of the IEEE/CVF conference on computer vision and pattern recognition*, pages 14902–14912, 2021. 6, 1
- [37] Yuyang Shi, Valentin De Bortoli, Andrew Campbell, and Arnaud Doucet. Diffusion schrödinger bridge matching. *Advances in Neural Information Processing Systems*, 36, 2024. 2
- [38] Javier Silvestre-Blanes, Teresa Albero-Albero, Ignacio Miralles, Rubén Pérez-Llorens, and Jorge Moreno. A public fabric database for defect detection methods and results. *Autex Research Journal*, 19(4):363–374, 2019. 6, 1
- [39] Jihoon Tack, Sangwoo Mo, Jongheon Jeong, and Jinwoo Shin. Csi: Novelty detection via contrastive learning on distributionally shifted instances. *Advances in neural information processing systems*, 33:11839–11852, 2020. 6
- [40] Matthias Wieler and Tobias Hahn. Weakly supervised learning for industrial optical inspection. In *DAGM symposium in*, page 11, 2007. 6, 1
- [41] Xincheng Yao, Ruoqi Li, Jing Zhang, Jun Sun, and Chongyang Zhang. Explicit boundary guided semi-push-pull contrastive learning for supervised anomaly detection. In *Proceedings of the IEEE/CVF Conference on Computer Vision and Pattern Recognition*, pages 24490–24499, 2023. 1, 2
- [42] Xincheng Yao, Ruoqi Li, Zefeng Qian, Lu Wang, and Chongyang Zhang. Hierarchical gaussian mixture normalizing flow modeling for unified anomaly detection. *arXiv preprint arXiv:2403.13349*, 2024. 1
- [43] Sangdoon Yun, Dongyoon Han, Seong Joon Oh, Sanghyuk Chun, Junsuk Choe, and Youngjoon Yoo. Cutmix: Regularization strategy to train strong classifiers with localizable features. In *Proceedings of the IEEE/CVF international conference on computer vision*, pages 6023–6032, 2019. 6
- [44] Qihang Zhou, Guansong Pang, Yu Tian, Shibo He, and Jiming Chen. Anomalyclip: Object-agnostic prompt learning for zero-shot anomaly detection. *arXiv preprint arXiv:2310.18961*, 2023. 1
- [45] Jiawen Zhu, Choubo Ding, Yu Tian, and Guansong Pang. Anomaly heterogeneity learning for open-set supervised anomaly detection. In *Proceedings of the IEEE/CVF Conference on Computer Vision and Pattern Recognition*, pages 17616–17626, 2024. 1, 2, 6, 7
- [46] Yuansheng Zhu, Wentao Bao, and Qi Yu. Towards open set video anomaly detection. In *European Conference on Computer Vision*, pages 395–412. Springer, 2022. 1, 2

Distribution Prototype Diffusion Learning for Open-set Supervised Anomaly Detection

Supplementary Material

7. Dataset Statistics

Extensive experiments are conducted on nine real-world anomaly detection (AD) datasets. Tab. 4 provides key statistics for all datasets used in this study. We follow the exact same settings as in previous open-set supervised anomaly detection (OSAD) studies. Specifically, for the MVTec AD dataset, we adhere to the original split, dividing the normal samples into training and test sets. For the other eight datasets, normal samples are randomly partitioned into training and test sets at a 3:1 ratio.

Table 4. The statistical information for nine real-world anomaly detection (AD) datasets, with the first 15 rows detailing the subsets of the MVTec AD dataset.

Dataset		Original Training		Original Test	
	C	Type	Normal	Normal	Anomaly
Carpet	5	Texttture	280	28	89
Grid	5	Texttture	264	21	57
Leather	5	Texttture	245	32	92
Tile	5	Texttture	230	33	83
Wood	5	Texttture	247	19	60
Bottle	3	Object	209	20	63
Capsule	5	Object	219	23	109
Pill	7	Object	267	26	141
Transistor	4	Object	213	60	40
Zipper	7	Object	240	32	119
Cable	8	Object	224	58	92
Hazelnut	4	Object	391	40	70
Metal_nut	4	Object	220	22	93
Screw	5	Object	320	41	119
Toothbrush	1	Object	60	12	30
MVTecAD	73	-	3629	467	1258
Optical	1	Object	10500	3500	2100
SDD	1	Texttture	594	286	54
AITEX	12	Texttture	1692	564	183
ELPV	2	Texttture	1131	377	715
Mastcam	11	Object	9302	426	451
Hyper-Kvasir	4	Medical	2021	674	757
BrainMRI	1	Medical	73	25	155
HeadCT	1	Medical	75	25	100

- MVTec AD [3] is a widely-used benchmark for defect detection, comprising 15 distinct categories, each of which includes one or several subcategories. The dataset contains a total of 73 fine-grained anomaly classes at either the texture or object level.
- Optical [40] is a synthetic dataset designed for industrial optical inspection and defect detection. The artificially

generated data mimics real-world tasks.

- SDD [?] is a defect product image detection dataset with pixel-level defect annotations. The original images, which have a resolution of 500×1250 , are vertically divided into three segments. Each segment is then annotated at the pixel level.
- AITEX [38] is a fabric defect detection dataset that includes 12 defect categories with pixel-level annotations. The original images, which have a resolution of 4096×256 , are cropped into multiple 256×256 patches. Each patch is then re-annotated at the pixel level.
- ELPV [8] is a dataset for defect detection in electroluminescence (EL) images of solar cells. It includes two types of defects, corresponding to different types of solar cells: monocrystalline and polycrystalline.
- Mastcam [13] is a novelty detection dataset constructed from geological images captured by the multispectral imaging system installed on the Mars rover. The dataset includes typical images and images from 11 novel geological classes. Each image comprises both shorter-wavelength (color) channels and longer-wavelength (grayscale) channels, with this study focusing on the shorter-wavelength channels.
- Hyper-Kvasir [4] is a large-scale, open-access gastrointestinal dataset collected during real endoscopy and colonoscopy procedures. It comprises four main categories and 23 subcategories of endoscopic and colonoscopic images. This work focuses on endoscopic images, where anatomical landmark categories are considered as normal samples and pathological categories are treated as abnormal samples.
- BrainMRI [36] is a brain tumor detection dataset obtained through magnetic resonance imaging (MRI).
- HeadCT [36] is a dataset for detecting intracranial hemorrhage obtained through head computed tomography (CT) scans.

8. Full Results under General Setting

Tab. 5 presents a comprehensive comparison of the proposed DPDL method with state-of-the-art (SOTA) approaches under general settings. It reports performance metrics for each category within the MVTec AD dataset. Overall, the DPDL model consistently outperforms baseline methods across all application scenarios in both ten-shot and one-shot settings, achieving the best performance in terms of Area Under the Curve (AUC).

Table 5. AUC performance (mean \pm std) across nine real-world AD datasets is reported under the general setting. **red** highlights the best results, and **blue** indicates sub-optimal outcomes. All baseline SOTA results are sourced from the original papers [9, 45].

Dataset	One Training Anomaly Example							Ten Training Anomaly Examples						
	DevNet	FLOS	SAOE	MLEP	DRA	AHL	DPDL (Ours)	DevNet	FLOS	SAOE	MLEP	DRA	AHL	DPDL (Ours)
Carpet	0.746 \pm 0.076	0.755 \pm 0.026	0.766 \pm 0.098	0.701 \pm 0.091	0.859 \pm 0.023	0.877 \pm 0.004	0.914 \pm 0.006	0.867 \pm 0.040	0.780 \pm 0.009	0.755 \pm 0.136	0.781 \pm 0.049	0.940 \pm 0.027	0.953 \pm 0.001	0.988 \pm 0.002
Grid	0.891 \pm 0.040	0.871 \pm 0.076	0.921 \pm 0.032	0.839 \pm 0.028	0.972 \pm 0.011	0.975 \pm 0.005	0.999 \pm 0.001	0.967 \pm 0.021	0.966 \pm 0.005	0.952 \pm 0.011	0.980 \pm 0.009	0.987 \pm 0.009	0.992 \pm 0.002	0.999 \pm 0.001
Leather	0.873 \pm 0.026	0.791 \pm 0.057	0.996 \pm 0.007	0.781 \pm 0.020	0.989 \pm 0.005	0.988 \pm 0.001	0.996 \pm 0.001	0.999 \pm 0.001	0.993 \pm 0.004	1.000 \pm 0.000	0.813 \pm 0.158	1.000 \pm 0.000	1.000 \pm 0.000	1.000 \pm 0.000
Tile	0.752 \pm 0.038	0.787 \pm 0.038	0.935 \pm 0.034	0.927 \pm 0.036	0.965 \pm 0.015	0.968 \pm 0.001	0.994 \pm 0.002	0.987 \pm 0.005	0.952 \pm 0.010	0.944 \pm 0.013	0.988 \pm 0.009	0.994 \pm 0.006	1.000 \pm 0.000	0.999 \pm 0.001
Wood	0.900 \pm 0.068	0.927 \pm 0.065	0.948 \pm 0.009	0.660 \pm 0.142	0.985 \pm 0.011	0.987 \pm 0.003	0.998 \pm 0.002	0.999 \pm 0.001	1.000 \pm 0.000	0.976 \pm 0.031	0.999 \pm 0.002	0.998 \pm 0.001	0.998 \pm 0.000	0.998 \pm 0.001
Bottle	0.976 \pm 0.006	0.975 \pm 0.023	0.989 \pm 0.019	0.927 \pm 0.090	1.000 \pm 0.000	1.000 \pm 0.000	1.000 \pm 0.000	0.993 \pm 0.008	0.995 \pm 0.002	0.998 \pm 0.003	0.981 \pm 0.004	1.000 \pm 0.000	1.000 \pm 0.000	1.000 \pm 0.000
Capsule	0.564 \pm 0.032	0.666 \pm 0.020	0.611 \pm 0.109	0.558 \pm 0.075	0.631 \pm 0.056	0.665 \pm 0.030	0.757 \pm 0.017	0.865 \pm 0.057	0.902 \pm 0.017	0.850 \pm 0.054	0.818 \pm 0.063	0.935 \pm 0.022	0.930 \pm 0.021	0.976 \pm 0.004
Pill	0.769 \pm 0.017	0.745 \pm 0.064	0.652 \pm 0.078	0.656 \pm 0.061	0.832 \pm 0.034	0.840 \pm 0.003	0.842 \pm 0.002	0.866 \pm 0.038	0.929 \pm 0.012	0.872 \pm 0.049	0.845 \pm 0.048	0.904 \pm 0.024	0.918 \pm 0.001	0.923 \pm 0.001
Transistor	0.722 \pm 0.032	0.709 \pm 0.041	0.680 \pm 0.182	0.695 \pm 0.124	0.668 \pm 0.068	0.796 \pm 0.003	0.748 \pm 0.002	0.924 \pm 0.027	0.862 \pm 0.037	0.860 \pm 0.053	0.927 \pm 0.043	0.915 \pm 0.025	0.926 \pm 0.009	0.928 \pm 0.001
Zipper	0.922 \pm 0.018	0.885 \pm 0.033	0.970 \pm 0.033	0.865 \pm 0.086	0.984 \pm 0.016	0.986 \pm 0.000	0.989 \pm 0.001	0.990 \pm 0.009	0.990 \pm 0.008	0.995 \pm 0.004	0.965 \pm 0.002	1.000 \pm 0.000	1.000 \pm 0.000	1.000 \pm 0.000
Cable	0.783 \pm 0.058	0.790 \pm 0.039	0.819 \pm 0.060	0.688 \pm 0.017	0.876 \pm 0.012	0.888 \pm 0.011	0.935 \pm 0.008	0.892 \pm 0.020	0.890 \pm 0.063	0.862 \pm 0.022	0.857 \pm 0.062	0.909 \pm 0.011	0.921 \pm 0.001	0.929 \pm 0.001
Hazelnut	0.979 \pm 0.010	0.976 \pm 0.021	0.961 \pm 0.042	0.704 \pm 0.090	0.977 \pm 0.030	0.984 \pm 0.004	0.997 \pm 0.002	1.000 \pm 0.000	1.000 \pm 0.000	1.000 \pm 0.000	1.000 \pm 0.000	1.000 \pm 0.000	1.000 \pm 0.000	1.000 \pm 0.000
Metal_nut	0.876 \pm 0.007	0.930 \pm 0.022	0.922 \pm 0.033	0.878 \pm 0.038	0.948 \pm 0.046	0.952 \pm 0.003	0.948 \pm 0.007	0.991 \pm 0.006	0.984 \pm 0.004	0.976 \pm 0.013	0.974 \pm 0.009	0.997 \pm 0.002	0.998 \pm 0.000	0.996 \pm 0.001
Screw	0.399 \pm 0.187	0.337 \pm 0.091	0.653 \pm 0.074	0.675 \pm 0.294	0.903 \pm 0.064	0.927 \pm 0.009	0.977 \pm 0.004	0.970 \pm 0.015	0.940 \pm 0.017	0.975 \pm 0.023	0.899 \pm 0.039	0.977 \pm 0.009	0.985 \pm 0.002	0.995 \pm 0.001
Toothbrush	0.753 \pm 0.027	0.731 \pm 0.028	0.686 \pm 0.110	0.617 \pm 0.058	0.650 \pm 0.029	0.794 \pm 0.016	0.807 \pm 0.001	0.860 \pm 0.066	0.900 \pm 0.008	0.865 \pm 0.062	0.783 \pm 0.048	0.826 \pm 0.021	0.921 \pm 0.007	0.929 \pm 0.000
MVTEC AD	0.780 \pm 0.020	0.755 \pm 0.136	0.834 \pm 0.007	0.744 \pm 0.019	0.883 \pm 0.008	0.901 \pm 0.003	0.927 \pm 0.002	0.945 \pm 0.004	0.939 \pm 0.007	0.926 \pm 0.010	0.907 \pm 0.005	0.959 \pm 0.003	0.970 \pm 0.002	0.977 \pm 0.002
Optical	0.523 \pm 0.003	0.518 \pm 0.003	0.815 \pm 0.014	0.516 \pm 0.009	0.888 \pm 0.012	0.888 \pm 0.007	0.915 \pm 0.002	0.782 \pm 0.065	0.720 \pm 0.055	0.941 \pm 0.013	0.740 \pm 0.039	0.965 \pm 0.006	0.976 \pm 0.004	0.983 \pm 0.005
SDD	0.881 \pm 0.009	0.840 \pm 0.043	0.781 \pm 0.009	0.811 \pm 0.045	0.859 \pm 0.014	0.909 \pm 0.001	0.917 \pm 0.003	0.988 \pm 0.006	0.967 \pm 0.018	0.955 \pm 0.020	0.983 \pm 0.013	0.991 \pm 0.005	0.991 \pm 0.001	0.996 \pm 0.001
AITEX	0.598 \pm 0.070	0.538 \pm 0.073	0.675 \pm 0.094	0.564 \pm 0.055	0.692 \pm 0.124	0.734 \pm 0.008	0.838 \pm 0.008	0.887 \pm 0.013	0.841 \pm 0.049	0.874 \pm 0.024	0.867 \pm 0.037	0.893 \pm 0.017	0.925 \pm 0.013	0.975 \pm 0.007
ELPV	0.514 \pm 0.076	0.457 \pm 0.056	0.635 \pm 0.092	0.578 \pm 0.062	0.675 \pm 0.024	0.828 \pm 0.005	0.897 \pm 0.002	0.846 \pm 0.022	0.818 \pm 0.032	0.793 \pm 0.047	0.794 \pm 0.047	0.845 \pm 0.013	0.850 \pm 0.004	0.937 \pm 0.003
Mastcam	0.595 \pm 0.016	0.542 \pm 0.017	0.662 \pm 0.018	0.625 \pm 0.045	0.692 \pm 0.058	0.743 \pm 0.003	0.838 \pm 0.011	0.790 \pm 0.021	0.703 \pm 0.029	0.810 \pm 0.029	0.798 \pm 0.026	0.848 \pm 0.008	0.850 \pm 0.005	0.934 \pm 0.010
Hyper-Kvasir	0.653 \pm 0.017	0.668 \pm 0.004	0.498 \pm 0.100	0.445 \pm 0.040	0.690 \pm 0.017	0.768 \pm 0.015	0.821 \pm 0.007	0.829 \pm 0.018	0.773 \pm 0.029	0.666 \pm 0.050	0.600 \pm 0.069	0.834 \pm 0.004	0.880 \pm 0.003	0.939 \pm 0.005
BrainMRI	0.694 \pm 0.004	0.693 \pm 0.036	0.531 \pm 0.060	0.632 \pm 0.017	0.744 \pm 0.004	0.866 \pm 0.004	0.893 \pm 0.004	0.958 \pm 0.012	0.955 \pm 0.011	0.900 \pm 0.041	0.959 \pm 0.011	0.970 \pm 0.003	0.977 \pm 0.001	0.969 \pm 0.005
HeadCT	0.742 \pm 0.076	0.698 \pm 0.092	0.597 \pm 0.022	0.758 \pm 0.038	0.796 \pm 0.105	0.825 \pm 0.014	0.865 \pm 0.005	0.982 \pm 0.009	0.971 \pm 0.004	0.935 \pm 0.021	0.972 \pm 0.014	0.972 \pm 0.002	0.999 \pm 0.003	0.981 \pm 0.003

Table 6. Detailed class-level AUC results (mean \pm std) under the hard setting. The best and second-best results are highlighted in **red** and **blue**, respectively. Carpet and Metal_nut are subsets of MVTEC AD.

Dataset	Class	One Training Anomaly Example							Ten Training Anomaly Examples						
		DevNet	FLOS	SAOE	MLEP	DRA	AHL	DPDL (Ours)	DevNet	FLOS	SAOE	MLEP	DRA	AHL	DPDL (Ours)
Carpet	Color	0.716 \pm 0.085	0.467 \pm 0.278	0.763 \pm 0.100	0.547 \pm 0.056	0.879 \pm 0.021	0.894 \pm 0.004	0.909 \pm 0.001	0.767 \pm 0.015	0.760 \pm 0.005	0.467 \pm 0.067	0.698 \pm 0.025	0.886 \pm 0.042	0.929 \pm 0.007	0.933 \pm 0.002
	Cut	0.666 \pm 0.035	0.685 \pm 0.007	0.664 \pm 0.165	0.658 \pm 0.056	0.902 \pm 0.033	0.934 \pm 0.003	0.941 \pm 0.003	0.819 \pm 0.037	0.688 \pm 0.059	0.793 \pm 0.175	0.653 \pm 0.120	0.922 \pm 0.038	0.943 \pm 0.002	0.951 \pm 0.004
	Hole	0.721 \pm 0.067	0.594 \pm 0.142	0.772 \pm 0.071	0.653 \pm 0.065	0.901 \pm 0.033	0.935 \pm 0.014	0.945 \pm 0.009	0.814 \pm 0.038	0.733 \pm 0.014	0.831 \pm 0.125	0.674 \pm 0.076	0.947 \pm 0.016	0.960 \pm 0.003	0.964 \pm 0.003
	Metal	0.819 \pm 0.032	0.701 \pm 0.028	0.780 \pm 0.172	0.706 \pm 0.047	0.871 \pm 0.037	0.931 \pm 0.007	0.940 \pm 0.001	0.863 \pm 0.022	0.678 \pm 0.083	0.883 \pm 0.043	0.764 \pm 0.061	0.933 \pm 0.022	0.921 \pm 0.003	0.938 \pm 0.005
	Thread	0.912 \pm 0.044	0.941 \pm 0.005	0.787 \pm 0.204	0.831 \pm 0.117	0.950 \pm 0.029	0.966 \pm 0.005	0.970 \pm 0.002	0.972 \pm 0.009	0.946 \pm 0.005	0.831 \pm 0.297	0.967 \pm 0.006	0.989 \pm 0.004	0.991 \pm 0.001	0.993 \pm 0.000
	Mean	0.767 \pm 0.018	0.678 \pm 0.040	0.753 \pm 0.055	0.679 \pm 0.029	0.901 \pm 0.006	0.932 \pm 0.003	0.941 \pm 0.006	0.847 \pm 0.017	0.761 \pm 0.012	0.762 \pm 0.073	0.751 \pm 0.023	0.935 \pm 0.013	0.949 \pm 0.002	0.956 \pm 0.004
Metal_nut	Bent	0.797 \pm 0.048	0.851 \pm 0.046	0.864 \pm 0.032	0.743 \pm 0.013	0.952 \pm 0.020	0.954 \pm 0.003	0.958 \pm 0.001	0.904 \pm 0.022	0.827 \pm 0.075	0.901 \pm 0.023	0.956 \pm 0.013	0.990 \pm 0.003	0.989 \pm 0.000	0.991 \pm 0.002
	Color	0.909 \pm 0.023	0.821 \pm 0.059	0.857 \pm 0.037	0.835 \pm 0.075	0.946 \pm 0.023	0.933 \pm 0.008	0.938 \pm 0.003	0.978 \pm 0.016	0.978 \pm 0.008	0.879 \pm 0.018	0.945 \pm 0.039	0.967 \pm 0.011	0.958 \pm 0.001	0.969 \pm 0.005
	Flip	0.764 \pm 0.014	0.799 \pm 0.058	0.751 \pm 0.090	0.813 \pm 0.031	0.921 \pm 0.029	0.931 \pm 0.002	0.940 \pm 0.004	0.987 \pm 0.004	0.942 \pm 0.009	0.795 \pm 0.062	0.805 \pm 0.057	0.913 \pm 0.021	0.937 \pm 0.003	0.953 \pm 0.003
	Scratch	0.952													

10. The Algorithm of DPDL

Algorithm 1 Distribution Prototype Diffusion Learning

- 1: **Input:** Input $\mathcal{X} = \{(x_i, y_i)\}$, C , ϵ , κ
 - 2: **for** $epoch = 1$ to n **do**
 - 3: Extract features $\mathcal{F} \xleftarrow{\text{feature}} \mathcal{X}$
 - 4: Distribution of normal samples transform $\mathcal{P}_{\text{MGP}} \xleftarrow{\text{bridge}} P(\mathcal{F})$
 - 5: Distribution Prototype Learning $\mathcal{L}_{\text{DPL}} = \mathcal{L}_{\text{DPL}}^n + \mathcal{L}_{\text{DPL}}^a$
 - 6: Dispersion Feature Learning \mathcal{L}_{DFL}
 - 7: Sample $\mathbf{x}_i \sim \mathcal{X}$, $\mathbf{e}_{e^*} \sim \mathcal{P}_{\text{MGP}}$
 - 8: Calculate scores $S_a \leftarrow M_a$, $S_n \leftarrow M_n$, $S_r \leftarrow M_r$
 - 9: **end for**
 - 10: **Output :** Anomaly score $S \leftarrow S_r + S_a - S_n$
-

11. Derivation of Eqns. (13) and (14)

We use Eqns. (8) and (12) to derive Eqn. (13) as follows:

$$\begin{aligned}
\pi(\psi(\mathbf{x}_i^n)|\mathbf{x}_i^n) &= \frac{1}{\varpi(\mathbf{x}_i^n)} \exp\left(\frac{\langle \mathbf{x}_i^n, \psi(\mathbf{x}_i^n) \rangle}{\epsilon}\right) \sum_{c=1}^C \alpha_c \mathcal{N}(\psi(\mathbf{x}_i^n); \boldsymbol{\mu}_c, \boldsymbol{\sigma}_c) \\
&= \frac{1}{\varpi(\mathbf{x}_i^n)} \sum_{c=1}^C \alpha_c (2\pi)^{-D/2} |\boldsymbol{\sigma}_c|^{-1/2} \exp\left(\frac{\langle \mathbf{x}_i^n, \psi(\mathbf{x}_i^n) \rangle}{\epsilon}\right) \exp\left(-\frac{1}{2} (\psi(\mathbf{x}_i^n))^\top \boldsymbol{\sigma}_c^{-1} (\psi(\mathbf{x}_i^n) - \boldsymbol{\mu}_c)\right) \\
&= \frac{1}{\varpi(\mathbf{x}_i^n)} \sum_{c=1}^C \alpha_c (2\pi)^{-D/2} |\boldsymbol{\sigma}_c|^{-1/2} \exp\left(\frac{1}{2\epsilon} (2\mathbf{x}_i^n^\top \psi(\mathbf{x}_i^n) - \psi(\mathbf{x}_i^n)^\top \boldsymbol{\sigma}_c^{-1} \psi(\mathbf{x}_i^n) + 2\boldsymbol{\mu}_c^\top \boldsymbol{\sigma}_c^{-1} \psi(\mathbf{x}_i^n) - \boldsymbol{\mu}_c^\top \boldsymbol{\sigma}_c^{-1} \boldsymbol{\mu}_c)\right) \\
&= \frac{1}{\varpi(\mathbf{x}_i^n)} \sum_{c=1}^C \alpha_c (2\pi)^{-D/2} |\boldsymbol{\sigma}_c|^{-1/2} \exp\left(\frac{1}{2\epsilon} (-\psi(\mathbf{x}_i^n)^\top \boldsymbol{\sigma}_c^{-1} \psi(\mathbf{x}_i^n) + 2 \underbrace{\left(\frac{1}{\epsilon} \boldsymbol{\sigma}_c \mathbf{x}_i^n + \boldsymbol{\mu}_c\right)^\top \boldsymbol{\sigma}_c^{-1} \psi(\mathbf{x}_i^n) - \boldsymbol{\mu}_c^\top \boldsymbol{\sigma}_c^{-1} \boldsymbol{\mu}_c}_{\tilde{\boldsymbol{\mu}}_c(\mathbf{x}_i^n)})\right) \\
&= \frac{1}{\varpi(\mathbf{x}_i^n)} \sum_{c=1}^C \alpha_c (2\pi)^{-D/2} |\boldsymbol{\sigma}_c|^{-1/2} \exp\left(-\frac{1}{2\epsilon} (\psi(\mathbf{x}_i^n) - \tilde{\boldsymbol{\mu}}_c(\mathbf{x}_i^n))^\top \boldsymbol{\sigma}_c^{-1} (\psi(\mathbf{x}_i^n) - \tilde{\boldsymbol{\mu}}_c(\mathbf{x}_i^n))\right) \\
&\exp\left(\frac{1}{2\epsilon} (-\boldsymbol{\mu}_c^\top \boldsymbol{\sigma}_c^{-1} \boldsymbol{\mu}_c + \tilde{\boldsymbol{\mu}}_c^\top(\mathbf{x}_i^n) \boldsymbol{\sigma}_c^{-1} \tilde{\boldsymbol{\mu}}_c^\top(\mathbf{x}_i^n))\right) \\
&= \frac{1}{\varpi(\mathbf{x}_i^n)} \sum_{c=1}^C \alpha_c \exp\left(\frac{\boldsymbol{\mu}_c^\top \boldsymbol{\sigma}_c^{-1} \boldsymbol{\mu}_c + (\tilde{\boldsymbol{\mu}}_c^\top \boldsymbol{\sigma}_c^{-1} \boldsymbol{\mu}_c + \tilde{\boldsymbol{\mu}}_c)^\top(\mathbf{x}_i^n) \boldsymbol{\sigma}_c^{-1} (\tilde{\boldsymbol{\mu}}_c^\top \boldsymbol{\sigma}_c^{-1} \boldsymbol{\mu}_c + \tilde{\boldsymbol{\mu}}_c)(\mathbf{x}_i^n)}{2\epsilon}\right) \mathcal{N}(\psi(\mathbf{x}_i^n); \tilde{\boldsymbol{\mu}}_c(\mathbf{x}_i^n), \boldsymbol{\sigma}_c) \\
&= \frac{1}{\varpi(\mathbf{x}_i^n)} \sum_{c=1}^C \alpha_c \exp\left(\frac{1}{2\epsilon^2} (\mathbf{x}_i^n)^\top \boldsymbol{\sigma}_c \mathbf{x}_i^n + \frac{1}{\epsilon} (\tilde{\boldsymbol{\mu}}_c)^\top(\mathbf{x}_i^n)\right) \mathcal{N}(\psi(\mathbf{x}_i^n); \tilde{\boldsymbol{\mu}}_c(\mathbf{x}_i^n), \boldsymbol{\sigma}_c) \\
&\quad \underbrace{\hspace{10em}}_{\tilde{\alpha}_c(\mathbf{x}_i^n)} \\
&= \tilde{\eta}(\mathbf{x}_i^n) \sum_{c=1}^C \tilde{\alpha}_c(\mathbf{x}_i^n) \mathcal{N}(\psi(\mathbf{x}_i^n); \tilde{\boldsymbol{\mu}}_c(\mathbf{x}_i^n), \boldsymbol{\sigma}_c)
\end{aligned}$$

where $\tilde{\eta}(\mathbf{x}_i^n) = \frac{1}{\varpi(\mathbf{x}_i^n)} = \frac{1}{\sum_{c=1}^C \tilde{\alpha}_c(\mathbf{x}_i^n)}$.

According to Eqn. (4), we derive Eqn. (14) as follows:

$$\begin{aligned}
g(\mathbf{x}_i^n, t) &= \epsilon \nabla_{\mathbf{x}_i^n} \log \int_{\mathbb{R}^D} \mathcal{N}(\psi(\mathbf{x}_i^n) | \mathbf{x}_i^n, (1-t)\epsilon \mathbf{I}) \exp\left(\frac{\|\psi(\mathbf{x}_i^n)\|^2}{2\epsilon}\right) \phi_1(\psi(\mathbf{x}_i^n)) d\psi(\mathbf{x}_i^n) \\
&= \epsilon \nabla_{\mathbf{x}_i^n} \log \int_{\mathbb{R}^D} \mathcal{N}(\psi(\mathbf{x}_i^n) | \mathbf{x}_i^n, (1-t)\epsilon \mathbf{I}) \exp\left(\frac{\|\psi(\mathbf{x}_i^n)\|^2}{2\epsilon}\right) \sum_{c=1}^C \alpha_c \mathcal{N}(\psi(\mathbf{x}_i^n); \tilde{\boldsymbol{\mu}}_c, \boldsymbol{\sigma}_c) d\psi(\mathbf{x}_i^n) \\
&= \epsilon \nabla_{\mathbf{x}_i^n} \log \left((2\pi)^{-\frac{D}{2}} |(1-t)\epsilon \mathbf{I}|^{-\frac{1}{2}} \sum_{c=1}^C \{\alpha_c |\boldsymbol{\sigma}_c|^{-\frac{1}{2}} \right. \\
&\quad \left. \int_{\mathbb{R}^D} \exp\left(-\frac{(\psi(\mathbf{x}_i^n) - \mathbf{x}_i^n)^\top (\psi(\mathbf{x}_i^n) - \mathbf{x}_i^n)}{2\epsilon(1-t)} - \frac{(\psi(\mathbf{x}_i^n) - \tilde{\boldsymbol{\mu}}_c)^\top \epsilon \boldsymbol{\sigma}_c^{-1} (\psi(\mathbf{x}_i^n) - \tilde{\boldsymbol{\mu}}_c)}{2\epsilon} + \frac{\psi(\mathbf{x}_i^n)^\top \psi(\mathbf{x}_i^n)}{2\epsilon}\right) \right\} \\
&= \epsilon \nabla_{\mathbf{x}_i^n} \log \left(\exp\left(-\frac{\mathbf{x}_i^n^\top \mathbf{x}_i^n}{2\epsilon(1-t)}\right) \sum_{c=1}^C \{\alpha_c |\boldsymbol{\sigma}_c|^{-\frac{1}{2}} \exp\left(-\frac{\tilde{\boldsymbol{\mu}}_c^\top \epsilon \boldsymbol{\sigma}_c^{-1} \tilde{\boldsymbol{\mu}}_c}{2\epsilon}\right)\} \right) \\
&\quad \int_{\mathbb{R}^D} \exp\left(-\frac{1}{2} [\psi(\mathbf{x}_i^n)^\top \underbrace{\left(\frac{t}{\epsilon(1-t)} \mathbf{I} + \boldsymbol{\sigma}_c^{-1}\right)}_{\boldsymbol{\Sigma}_c^t} \psi(\mathbf{x}_i^n)] + \underbrace{\left[\frac{1}{\epsilon(1-t)} \mathbf{x}_i^n + \boldsymbol{\sigma}_c^{-1} \tilde{\boldsymbol{\mu}}_c\right]^\top}_{h_c(\mathbf{x}_i^n, t)} \psi(\mathbf{x}_i^n)\right) d\psi(\mathbf{x}_i^n) \\
&= \epsilon \nabla_{\mathbf{x}_i^n} \log \left((2\pi)^{-\frac{D}{2}} \exp\left(-\frac{\mathbf{x}_i^n^\top \mathbf{x}_i^n}{2\epsilon(1-t)}\right) \sum_{c=1}^C \underbrace{\{\alpha_c (2\pi)^{-\frac{D}{2}} |\boldsymbol{\sigma}_c|^{-\frac{1}{2}} \exp\left(-\frac{\tilde{\boldsymbol{\mu}}_c^\top \epsilon \boldsymbol{\sigma}_c^{-1} \tilde{\boldsymbol{\mu}}_c}{2\epsilon}\right)\}}_{\mathcal{N}(\mathbf{x}_i^n | 0, \epsilon(1-t)\mathbf{I})} \right) \\
&\quad \underbrace{\sum_{c=1}^C \{\alpha_c \mathcal{N}(\tilde{\boldsymbol{\mu}}_c(\mathbf{x}_i^n) | \mathbf{0}, \boldsymbol{\sigma}_c) \mathcal{N}(h_c(\mathbf{x}_i^n, t) | 0, \boldsymbol{\Sigma}_c^t)\}}_{\rho_{\text{MGP}}(\mathbf{x}_i^n)} \\
&= \epsilon \rho_{\text{MGP}}(\mathbf{x}_i^n) \nabla_{\mathbf{x}_i^n} \log(\mathcal{N}(\mathbf{x}_i^n | 0, \epsilon(1-t)\mathbf{I}))
\end{aligned}$$